PNAS RESEARCH ARTICLE | PHYSICS

Hydrodynamic coupling melts acoustically levitated crystalline rafts

Brady Wu[a,b,1], Bryan VanSaders[a,b], Melody X. Lim[a,b,2], and Heinrich M. Jaeger[a,b]

Edited by Steve Granick, Institute for Basic Science, Ulju-gun, Ulsan, Korea (South); received January 30, 2023; accepted June 6, 2023

Going beyond the manipulation of individual particles, first steps have recently been undertaken with acoustic levitation in air to investigate the collective dynamical properties of many-body systems self-assembled within the levitation plane. However, these assemblies have been limited to two-dimensional, close-packed rafts where forces due to scattered sound pull particles into direct frictional contact. Here, we overcome this restriction using particles small enough that the viscosity of air establishes a repulsive streaming flow at close range. By tuning the particle size relative to the characteristic length scale for viscous streaming, we control the interplay between attractive and repulsive forces and show how particles can be assembled into monolayer lattices with tunable spacing. While the strength of the levitating sound field does not affect the particles' steady-state separation, it controls the emergence of spontaneous excitations that can drive particle rearrangements in an effectively dissipationless, underdamped environment. Under the action of these excitations, a quiescent particle lattice transitions from a predominantly crystalline structure to a two-dimensional liquid-like state. We find that this transition is characterized by dynamic heterogeneity and intermittency, involving cooperative particle movements that remove the timescale associated with caging for the crystalline lattice. These results shed light on the nature of athermal excitations and instabilities that can arise from strong hydrodynamic coupling among interacting particles.

acoustic levitation | hydrodynamic instability | order-to-disorder transition | intermittency | strongly coupled systems

Significance

Acoustic levitation provides a versatile platform for contactless manipulation of small, subwavelength particles. Until now, simultaneous levitation of multiple strongly interacting particles has been restricted to configurations where the particles are in direct contact, a source of significant dissipation. Levitating in a regime where repulsive viscosity-driven interactions balance attractive acoustic forces makes it possible to form assemblies where particles are closely spaced with tunable stable separation. This opens up opportunities to investigate the complex dynamics arising from strong hydrodynamic interactions in driven, underdamped, many-body systems.

Acoustic levitation is a widely used contact-free technique to manipulate particles and direct their assembly (1–9). More recently, it has also been used to study the collective properties of interacting many-particle systems (10–13). Within the nodal plane of an acoustic cavity, scattered sound waves establish tunable attractions between particles (14), aggregating them together. While submillimeter granular particles are too large for thermal noise to drive their dynamics, athermal fluctuations can be introduced by slightly detuning the cavity excitation away from its resonant frequency, which results in spontaneous vertical oscillations (10, 15, 16) or rotations of an entire monolayer raft (11). Such fluctuations are a manifestation of hydrodynamic instabilities, where the configuration of particles moving relative to a surrounding fluid evolves unpredictably due to hydrodynamic coupling.

Excitations induced by hydrodynamic instabilities in many-body systems can exhibit complex correlations that control collective properties, in contrast to uncorrelated thermal fluctuations. In the above-mentioned prior work, the fluctuations emerged from feedback between a moving object and the acoustic cavity mode, an instability found already for a single levitated particle (15, 16). A more subtle instability can arise from the hydrodynamic coupling among multiple particles. For example, such hydrodynamic instabilities can occur among neighboring particles settling in a fluid (17, 18) and have been associated with the chaotic trajectories of small numbers of weakly interacting steel spheres in an oscillating glycerol bath (19). Acoustic levitation would, in principle, be a powerful technique to study these hydrodynamic instabilities in extended systems of hundreds of particles evolving over long time scales if direct contact due to purely attractive interactions could be avoided. However, in prior studies (10, 11), frictional, and thus strongly dissipative, particle contacts masked the presence of hydrodynamic instabilities arising from the relative motion of particles.

We circumvent this limitation by levitating particles in a regime where a viscosity-driven repulsive streaming flow can have an appreciable effect on the structure of the particle assembly. When the levitated particles become comparable in size to the extent of the streaming flows, the repulsive hydrodynamic forces can counteract attractive scattering forces at close range. By tuning the particle size, and by extension,

Author affiliations: [a]Department of Physics, University of Chicago, Chicago, IL 60637; and [b]James Franck Institute, University of Chicago, Chicago, IL 60637

Author contributions: B.W., B.V., M.X.L., and H.M.J. designed research; B.W. and B.V. performed research; B.W. and B.V. analyzed data; and B.W., B.V., M.X.L., and H.M.J. wrote the paper.

The authors declare no competing interest.

This article is a PNAS Direct Submission.

[1]To whom correspondence may be addressed. Email: bwu34@uchicago.edu.

[2]Present address: Laboratory of Solid State and Atomic Physics, Cornell University, Ithaca, NY 14853.

This article contains supporting information online at https://www.pnas.org/lookup/suppl/doi:10.1073/pnas.2301625120/-/DCSupplemental.

Published July 10, 2023.

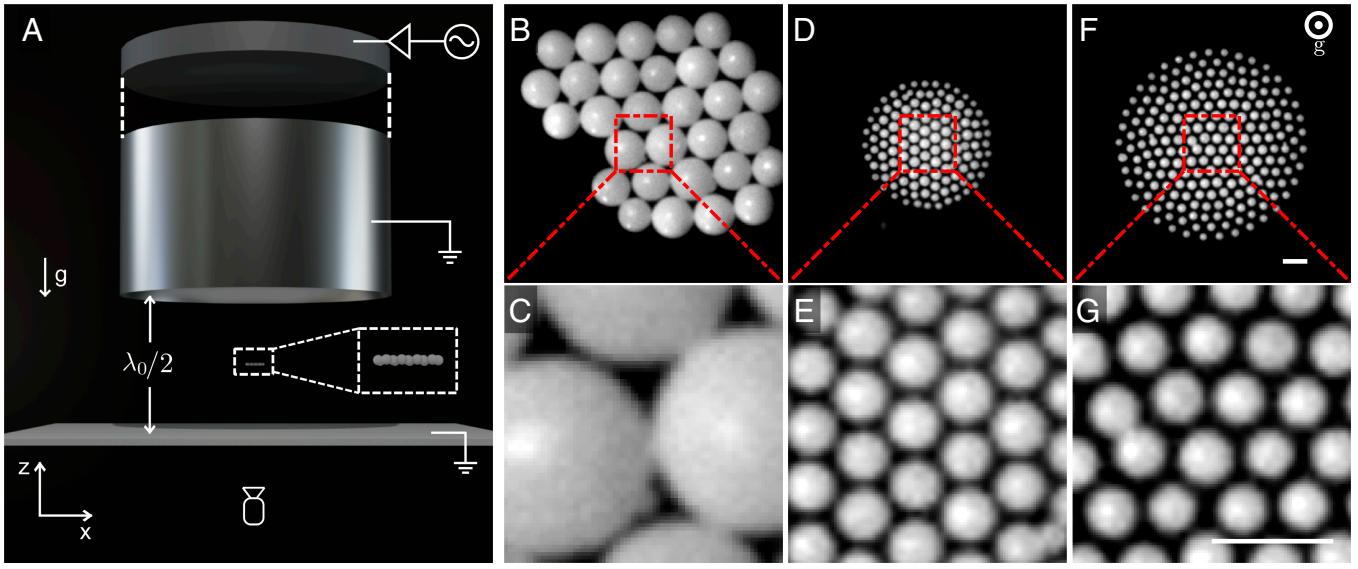

Fig. 1. Acoustically levitated particles with tunable interactions. (*A*) Schematic of the experimental setup. A single-axis transducer consisting of a piezoelectric driving element coupled to an aluminum horn generates ultrasonic standing waves in the gap (adjusted to half the resonant sound wavelength λ_0) between the bottom of the horn and a reflecting, optically transparent surface. Particles are levitated at the pressure nodal plane in the middle of the gap and imaged with a high-speed video camera from below. (*B*–*G*) Images of levitated particle rafts (*Top*) and zoomed-in views (*Bottom*). The particles have average diameters $D = 180$ μm (*B* and *C*) and $D = 40$ μm (*D*–*G*) and are levitated with frequency $\omega/(2\pi) = 34.7$ kHz ($\lambda = 9.9$ mm) (*B*, *C*, *F*, and *G*) and $\omega/(2\pi) = 64.3$ kHz ($\lambda = 5.3$ mm) (*D* and *E*). (All scale bars are 100 μm.)

the relative strengths of attraction and repulsion, we are able to vary the steady-state distance between pairs of levitated particles from direct contact to well separated (Fig. 1). In this contactless levitation regime, particle assemblies exhibit a range of dynamical behaviors associated with underdamped, strongly coupled many-body systems, as observed, for example, in cold dusty plasmas (20–25), but here driven by hydrodynamic interactions.

While the particle steady-state separation resulting from the force balance does not depend on the energy density in the acoustic cavity, we find that the sound energy determines the magnitude of hydrodynamic instability-driven excitations, controlling the transition from a quiescent crystal-like state to a highly diffusive liquid-like state. As a result of fluid-induced spatiotemporal correlations, this transition is mediated by intermittent, avalanche-like dynamics where a single local displacement event can trigger system-wide rearrangements, a clear distinction from the standard picture of a spatially homogeneous thermal melting transition (26, 27). In levitated rafts, the avalanche-like excitations are found to arise as a consequence of correlated motion between neighboring particles, starting from the ballistic time scale, which produces a crystal lacking a characteristic caging time scale. These excitations resemble the string-like cooperative motions found during the premelting of solids (28), in the interfacial region of ice (29), or in dusty plasma systems (20–23).

Our experimental setup is illustrated in Fig. 1*A*. A resonating acoustic cavity is formed by the gap between an ultrasonic transducer and a reflecting surface. The resonant frequency $\omega_0/(2\pi)$ of the transducer is 34,870 Hz, with an associated free space wavelength $\lambda_0 = 2\pi c/\omega_0 \simeq 9.8$ mm, where c is the speed of sound in air (*SI Appendix*, Fig. S1). The gap height between the transducer and the reflector is kept constant at $\lambda_0/2 = 4.9$ mm for all experiments. Here, we use polyethylene particles of diameter $D = 30$ to 60 μm (*SI Appendix*, Figs. S2 and S3), such that the setup operates deep in the Rayleigh scattering regime ($\lambda \gg D$). Unlike larger levitated objects (10, 15, 16), these particles comprise a negligible volume fraction of the resonating cavity. As a result, changing the driving frequency ω or amplitude adjusts the energy density of the acoustic cavity without triggering spontaneous vertical oscillations of individual particles. Confined by single-scattering forces (i.e., primary forces) (30, 31), particles levitate at the pressure nodal plane and are imaged from below using a high-speed camera (Fig. 1 *B*–*G*).

Tunable Attractive and Repulsive Interactions

At low energy density in the cavity, particles levitate in stationary configurations and do not fluctuate. The steady-state distances between particles are determined by the competition of attractive and repulsive interparticle forces. Attractive forces arise from the scattering of sound between particles. These long-range secondary radiation forces are anisotropic, with attraction for particle configurations in the nodal plane and repulsion out of the plane (14) (Fig. 2*A*). The magnitude of in-plane attraction as a function of distance scales as

$$F_{sc}(r) \propto -\frac{E_0 D^6}{r^4}, \qquad [1]$$

where $E_0 \equiv p_{ac}^2/(2\rho_0 c^2)$ is the energy density of the acoustic field in air with pressure amplitude p_{ac}, density ρ_0, and r is the center-to-center distance between particles of diameter D (14). In our experiments, we measure the amplitude of the acoustic pressure wave p_{ac} with an optical microphone (*Materials and Methods*), which we refer to as acoustic pressure.

Interparticle repulsion arises from the viscosity of the embedding medium (air) and is not captured by the above scattering analysis. Near particle surfaces, a viscous boundary layer of characteristic thickness $\delta_\nu = \sqrt{2\nu/\omega}$ forms, over which the velocity of air relative to the particle surface decays to zero. Here, ν is the kinematic viscosity. For $\omega = \omega_0$, $\delta_\nu \approx 12$ μm in air. Within the boundary layer, acoustic energy is coupled to steady, short-ranged flows. For particle sizes much larger than δ_ν, the influence of this boundary layer is negligible; however,

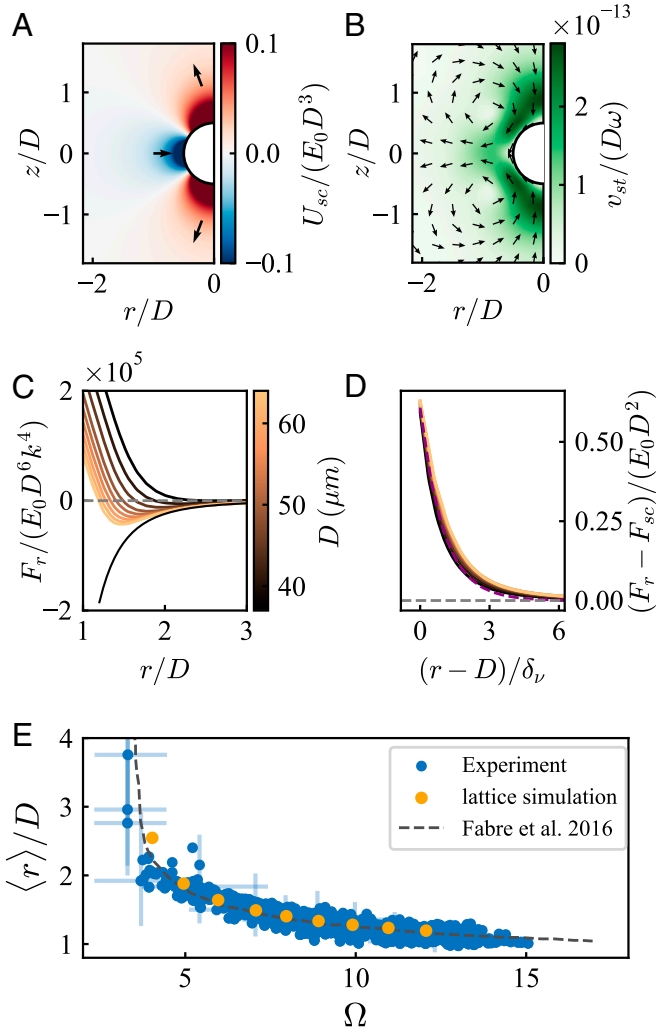

Fig. 2. Short-ranged repulsive interactions from viscous effects. (*A*) Acoustic scattering potential, U_{SC}, in the *x*–*z* plane. The interaction is attractive in the equatorial and repulsive in the polar direction. The white circle represents the particle. (*B*) Time-averaged microstreaming flow of magnitude v_{st} in the *x*–*z* plane around a 45-μm sphere levitated at $\omega/(2\pi) = 34.7$ kHz, obtained from COMSOL simulation. The direction of flow-induced forces in the levitation plane is opposite to that in *A*. (*C*) Magnitude of the net force in the equatorial direction F_r as a function of radial distance *r* for various particle diameters *D*, from lattice fluid simulation. Here, $k = 2\pi/\lambda$, where λ is the wavelength of the generated acoustic wave. The black curve represents the force from the scattering expansion following ref. 14. (*D*) Magnitude of the microstreaming repulsive interaction, approximated by subtracting the scattering expansion from the net force in *C*. The purple dashed line represents an exponential decay, $exp(-(r-D)/\delta_\nu)$, with $\delta_\nu = 12$ μm. (*E*) Time-averaged steady-state separation $\langle r \rangle/D$ for a particle pair as function of Stokes number Ω. Blue errorbars represent the uncertainties for selected data points (*SI Appendix*, Fig. S2).

for $D \approx \delta_\nu$, the time-averaged, nonlinear microstreaming flows that develop within the viscous boundary layer surrounding the particle become significant. These flows form two toroidal vortices around the sphere, aligned with the axis of the exciting wave (32). Flow in the levitation plane near the particle surface is outward, opposing attraction from the radiation force (Fig. 2*B*).

We calculate interparticle forces using the lattice Boltzmann method (LBM), a discretized direct fluid simulation technique, and microstreaming flow fields using COMSOL (*Materials and Methods*). Fig. 2*C* shows the force experienced between pairs of variously sized particles, scaled by the nondimensional prefactor of the scattering expansion pair interaction. For $r/D > 2$, pair forces are attractive for most sizes, and larger particles more closely follow the form of the scattering expansion (black curve). We estimate the form of the viscous repulsive interaction by subtracting the scattering expansion from the net force, yielding the data in Fig. 2*D*.

The length scale of this microstreaming-induced repulsion depends primarily on δ_ν (which is similar for particles of all sizes at the same driving frequency ω), and the magnitude scales as D^2. As radiation forces scale as D^6 (Eq. **1**), the relative magnitude of the viscous correction to the short-ranged interaction increases as particle size is decreased.

The competition between scattering and viscous forces produces in-plane stable separations which are controlled by the Stokes number $\Omega = \omega D^2/(4\nu)$ (33). Fig. 2*E* compares the numerical results for the steady state, in-plane center-to-center particle distance $\langle r \rangle$ from Fabre et al. (33) with our LBM simulations and experimental observations, showing close agreement. Importantly, we find no significant difference in $\langle r \rangle$ when comparing isolated particle pairs with pairs of neighboring particles inside large rafts (*SI Appendix*, Fig. S4). In addition, since the magnitude of both the attractive radiation force and the repulsive streaming-induced force scale linearly with E_0, $\langle r \rangle$ does not depend on the energy density of the cavity (*SI Appendix*, Fig. S4). These results are consistent with prior investigations of centimeter-scale spherical particles in a confined, oscillating viscous liquid (19, 34–36).

A consequence of the above relation between $\langle r \rangle$ and Ω is a size sorting effect, in which small particles gather near the raft edge (Fig. 1*F* and *SI Appendix*, Fig. S5*B*). Having the smaller particles, with their larger interparticle separations $\langle r \rangle$, near the edge minimizes the raft area. Our subsequent analysis focuses on the central region of the raft.

Nonreciprocal Multibody Acoustic Interaction

While the acoustic interaction between two levitated particles is reciprocal and conservative (Fig. 2) (14, 31), hydrodynamic interactions between many particles can be distinctly nonconservative, injecting energy into particle degrees of freedom (37). To demonstrate this, we simulate a compact, seven-particle cluster composed of one central particle surrounded by a hexagonal ring of neighbors interacting via a lattice fluid. Particle separations are chosen so that forces are balanced in the steady state; however, displacing the central particle a distance Δx along the *x* direction, while keeping all other particles fixed, breaks force balance (Fig. 3 *A*, *Insets*). Net forces on individual particles (f_i) are shown as black arrows.

As expected, forces on the central, displaced particle act to restore it to the force-balanced condition (black dashed outline). However, the sum of individual net forces ($\sum_i f_i$, Fig. 3*A*) has a nonzero magnitude that grows with increasing particle displacement. This is a clear signature of nonreciprocal (and therefore also nonconservative) interactions, in which Newton's third law ($f_{ij} = -f_{ji}$) is broken. This result can be contrasted with the net forces on the same particle configuration due to a pairwise LJ interaction (Fig. 3*B*), in which $\sum_i f_i = 0$ for all Δx. Additionally, we note the geometry of particle forces for acoustic interactions: Forces are not necessarily aligned with the vector between particle centers (Fig. 3*A*). For pairwise additive forces, particle interactions are independent, and so the net force on any particle in this cluster must point toward the displaced central particle (as for LJ forces in Fig. 3 *B*, *Insets*). This difference is a clear indication that acoustic forces have a

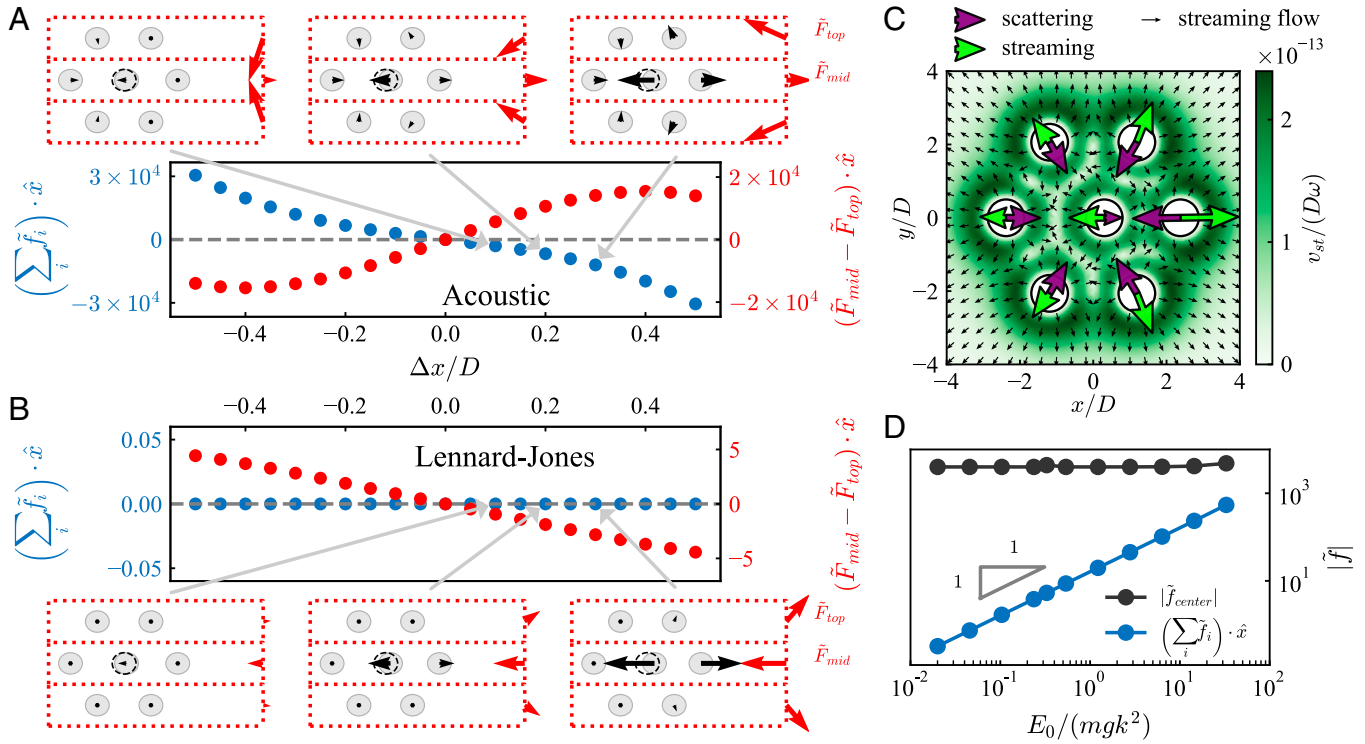

Fig. 3. Nonreciprocal and multibody effects in acoustic interactions. Net forces on individual and groups of particles in a levitated, seven-particle cluster, contrasted with a pair-wise additive interaction (the LJ force) on the same configuration. For acoustically interacting clusters, the displacement of a single particle from its force-balanced position leads to nonreciprocal forces that promote the shearing of close-packed layers. (*A*) Various forces (obtained from LBM simulation) in an acoustically interacting cluster as the central particle is displaced by an amount Δx from its stable position. Insets show individual forces (black) and net forces on layers parallel to the displacement direction (red, force scale eight times smaller than the black arrows). The sum of all individual forces is shown in the main panel (blue points), along with the difference of net forces on the top and middle layers (red points). Acoustic clusters have nonconservative forces that promote shearing of particle layers in the direction of point displacements. (*B*) The same configuration interacting through pair-wise additive LJ forces has no nonconservative force component (blue points) and the opposite behavior for layer shear forces (red points). Here, all forces act to restore the cluster toward its undisturbed configuration, unlike for particles interacting acoustically. (*C*) Time-averaged streaming flow of magnitude v_{st} around the minimal cluster in the *x*–*y* plane for $\Delta x/D = 0.3$, obtained from COMSOL simulation. Green and purple arrows denote the force contributed by viscous streaming repulsion and scattering attraction, respectively. (*D*) Magnitude of the net force from LBM simulation on the central, displaced particle (black) and the sum of net forces on all particles in the *x* direction (blue) for different acoustic energy density E_0 normalized by mgk^2, where $m = \pi\rho D^3/6$ and $g = 9.8$ m/s^2. As in Fig. 2*C*, all acoustic forces reported here are normalized as $\tilde{f}_i = f_i/(E_0 D^6 k^4)$, and Lennard-Jones (LJ) interactions are normalized as $\tilde{f}_i = f_i/(\epsilon/\sigma)$, where ϵ and σ are characteristic energy and length scale of the potential.

multibody character, in which the movement of particle 1 with respect to a stationary particle 2 also modifies the interaction of particle 2 with a nearby, undisturbed particle 3. Ultimately, this nonreciprocal, multibody interaction is of hydrodynamic origin: Displacement of the central particle modifies the secondary streaming flow profile around its neighbors (Fig. 3*C*), leading to forces on particles which cannot be described as additive functions of particle position alone (green and purple arrows stand for streaming and scattering forces, respectively; for more details, see *SI Appendix*, Fig. S6).

We can further examine the structure of these forces by dividing the cluster into three layers of particles parallel to Δx (Fig. 3*A*, red dashed boxes) and separately calculating the net forces acting on the top and middle layers, F_{top} and F_{mid}. These forces are shown in Fig. 3 as red arrows (scaled up eight times than the net forces on individual particles, f_i, shown in black). The force that drives these layers past each other in the *x* direction is $(F_{mid} - F_{top}) \cdot \hat{x}$, and for acoustic interactions, we find that this force has the same sign as the displacement of the central particle (Fig. 3*A*, red points). This is a counterintuitive finding, and it indicates that our acoustically interacting small cluster responds with collective forces that promote internal shear to move the displaced particle further in the direction of displacement relative to nearby layers. It implies that a local deformation leads to multibody forces that encourage strings of particles to move in a coordinated fashion. We can contrast this behavior with what would have resulted from conservative, pairwise additive forces based on LJ interactions (Fig. 3*B*). In that case, $(F_{mid} - F_{top}) \cdot \hat{x} \propto -\Delta x$, implying resistance to the displacement of the central particle.

Finally, we examine how these forces grow as the applied acoustic energy density is increased. The conservative and reciprocal forces that control interparticle spacing (Fig. 2 *C* and *D*) both scale linearly with the energy density E_0 of the acoustic environment. The net restoring force on the displaced center particle (f_{center}) is dominated by such forces, and so $|f_{center}|$ was also found to scale linearly with E_0 (Fig. 3*D*, black points, slope of zero due to normalization). However, the net force on the cluster $\sum_i f_i$ capable of energizing the system scales approximately as E_0^2 (Fig. 3*D*, blue points), as do the forces that drive layers to move past each other.

Taken together, the results presented in Fig. 3 predict that particles in acoustically levitated clusters will have strongly correlated motion. Furthermore, since the conservative interparticle forces scale linearly with the cavity energy density, whereas the nonreciprocal interparticle forces depend quadratically on the cavity energy density (Fig. 3*D*), as E_0 increases, the hydrodynamic instability-driven perturbations grow more rapidly than the

stabilizing conservative forces. To test these two predictions in larger systems, we now turn to experiments and show how the nonconservative forces can drive an order-to-disorder transition and "melt" a levitated granular crystal.

Order-to-Disorder Transition

In the following, we focus on levitated rafts with $\Omega \approx 6$ and increase E_0 by increasing p_{ac}. We observe that this drives a transition from quiescent crystal-like state (Fig. 4 *A*, *i* and Movie S1) with well-defined stable interparticle spacings, to liquid-like state (Fig. 4 *A*, *ii* and Movie S2) with rapidly fluctuating particle positions and associated increase in kinetic energy E_{kin} (Fig. 4*B*). Here, $E_{kin} = \langle mv_i^2/2 \rangle_N$ is defined as the translational kinetic energy per particle in the xy plane averaged over N particles in the system, where v_i is the velocity of particle i and $m = \pi\rho D^3/6$ is the average mass of the particles, taken as having diameter $D = 45$ μm and density $\rho = 1{,}000$ kgm^{-3}. We note that all particle motion in this liquid state occurs within the levitation plane and, within the spatial resolution of our experimental setup, does not involve excursions into the vertical direction (Movie S3).

The velocity distribution of the particles in the bulk of a raft is isotropic and well described as a granular gas (*SI Appendix*, Figs. S7 and S8). However, due to the presence of the boundary, particles near the raft edge are more constrained and have less freedom to move in the radial direction than the azimuthal direction, thus producing distinctive rings where particles rarely leave their respective annuli (*SI Appendix*, Figs. S8 and S9). Unlike most materials (which have positive coefficients of thermal expansion), the particle density in the raft stays nearly constant with increasing $\langle E_{kin} \rangle$, as can be observed in Fig. 4 *A*, *i* and *ii* and *SI Appendix*, Fig. S5*D*.

To quantify how disorder emerges in the crystal-like state as p_{ac} is increased, we calculate the spatially and long-time averaged bond order parameter $\Phi_6 = \langle \frac{1}{N_{nn}} \sum_{nn} e^{i6\theta_k} \rangle_N$, where θ_k is the angle between the bond and an arbitrary axis, *nn* denotes nearest neighbor, N_{nn} is the number of neighbor particles, and the average is over all particles N (26, 27). We find that Φ_6 monotonically decreases with increasing p_{ac} (Fig. 4*C*), as expected from Fig. 3*D*.

We find that this order-to-disorder transition is characterized by sudden, avalanche-like rearrangements (Fig. 5*A*). To quantify these excursions, we calculate a spatially averaged, local order correlation function, $h_6(t, \Delta t) = \langle \Phi_6(t - \Delta t) \cdot \Phi_6(t)^* \rangle_N$, which measures how much local sixfold orientational order (Φ_6) changed over a short time interval Δt before time t, averaged over N particles. $h_6 = 1$ indicates no change in ordering, while h_6 close to zero corresponds to the decorrelation of local bond order. A characteristic decorrelation time $\Delta t =$ 10 ms was chosen for the liquid state, but the behavior of h_6 shown here is not sensitive to choices of Δt from 5 to 100 ms.

Fig. 4*D* shows the evolution of h_6 for three representative cases. Rafts exhibit intermittent dynamics (orange), where $h_6(t)$ switches between low and high values at random intervals, indicating that the raft behaves as a crystal-like state with stochastic bursts of liquid-like rearrangements. The quiescent, crystal-like state has a wide range of lifetimes, from fractions of a second to a few seconds, but will eventually be interrupted by a liquid-like excitation. In the crystal-like state, the particle displacements are smaller than a lattice spacing and account for all decorrelations $h_6 > 0.9$ (red shaded band). For example, the dip in h_6 for the red trace around 0.3 s is due to phonon motion in an otherwise stationary crystal. Finally, at large p_{ac}, the raft enters a liquid-like state, with $h_6 < 0.5$. Defining the probability $P(crys)$ of finding the raft in the crystal-like state as the fraction of time that $h_6 > 0.9$, we observe a sharp drop around $p_{ac}^* \approx 860\ Pa = 1.1 p_{ac}^{min}$ (p_{ac}^* is the purple dashed line in Fig. 4 *B*, *C*, and *E*, $p_{ac}^{min} = 780$ Pa is the minimum pressure at which rafts can be stably levitated against gravity), signaling the transition from the stochastically interrupted crystal-like state, to a consistently liquid-like state.

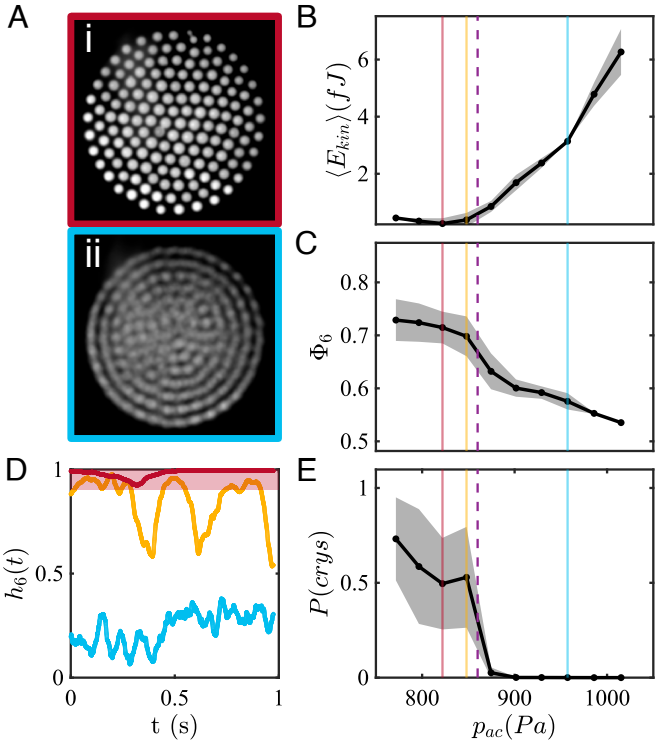

Fig. 4. Acoustic energy density controls crystal–liquid transition. (*A*) Time-averaged images of crystal-like (*i*) and liquid-like (*ii*) states over 167 ms at $p_{ac} = 822$ Pa and $p_{ac} = 957$ Pa. (*B* and *C*) Average kinetic energy per particle in the xy direction E_{kin}, and the bond order parameter Φ_6 as a function of acoustic pressure, p_{ac}, averaged over 1 s. (*D*) Bond correlation function $h_6(t) = \langle \Phi_6(t-\Delta t) \cdot \Phi_6(t) \rangle$ for crystal (maroon), liquid (blue), and intermittent dynamics (orange). $\Delta t = 10$ ms. We define $P(crys)$ as the probability of $h_6 > 0.9$ (the shaded region). (*E*) Probability of crystal-like state, $P(crys)$, as a function of p_{ac}.

Intermittent Dynamics from Cooperative Motion

We now look in more detail at the structural rearrangements that are produced by hydrodynamic instabilities inside a raft. Intermittent excursions into the liquid-like state can be identified by pulses in the kinetic energy per particle (Fig. 5 *A*, *Inset*), where each pulse is an intense, avalanche-like excitation. Between such events, the system settles into an idle, highly ordered crystal state (Movie S4). These excited and quiescent states exist for similar amounts of time and typically each last for a fraction of a second. At the onset of an event (Fig. 5*A* and Movie S5), the kinetic energy increases smoothly at about the same rate as it decays by viscous damping of individual particle motions in air. This similarity in the rates of energy increase and decrease implies that the energy is injected locally via the nonconservative hydrodynamic interactions of the type shown in Fig. 3*A*, on a per

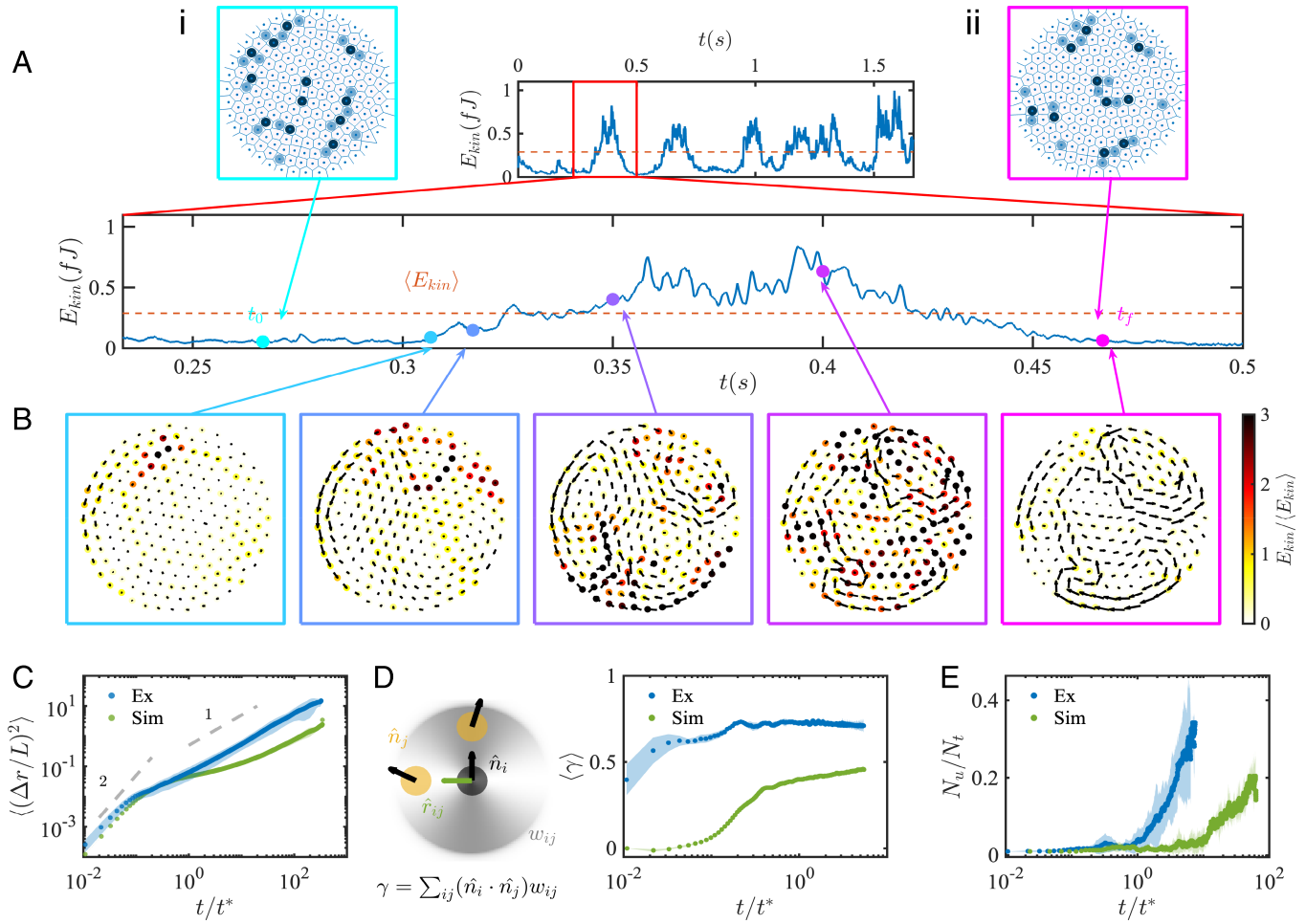

Fig. 5. Cooperative uncaging drives intermittent dynamics. (*A*) Kinetic energy per particle within a raft during a representative sequence of avalanches over a time span of 1.65 s, with zoomed-in detail for one avalanche (boxed in red). Dashed horizontal lines: kinetic energy per particle averaged over 10 s. Marked points correspond to the snapshots shown in *B*. *Insets i* and *ii*: Voronoi construction of the cluster configuration before and after the avalanche. Light and dark blue represent the defects with 5 and 7 neighbors. (*B*) Spatiotemporal evolution of the raft during the avalanche highlighted in *A*. Arrows denote the displacement field from time t_0 before the event. Particles are shown at their t_0 locations and colored with their current values of $E_{kin}/\langle E_{kin}\rangle$. (*C*) Normalized mean square displacement $\langle(\Delta r/L)^2\rangle$ as a function of normalized time t/t^* for both experiment and MD simulation. L denotes the lattice spacing, and $t^* = L/\langle v\rangle$. (*D*) Correlation parameter $\langle\gamma\rangle$ (Eq. **2**) as a function of t/t^*. The schematic shows the definition of γ, with angular weighting function $w_{ij} = (\hat{n}_i \cdot \hat{r}_{ij})^2$ depicted by the shaded area; directions parallel to the particle motion are weighted more heavily. (*E*) Fraction of uncaged particles in a raft, N_u/N_t, as a function of t/t^*. N_u and N_t are the uncaged and total particle number, respectively. A particle is considered uncaged if the displacement from time t_0 is greater than $\langle v\rangle t^*$. The shaded area represents the SD from 10 independent avalanche events in the same raft.

particle basis, rather than through a sudden external, boundary-coupled perturbation (e.g., via an air current).

To better understand these intermittent excursions, we next examine the per-particle dynamics of a representative event. We define a reference time t_0 immediately before the onset of the event for comparison with later times, t. In Fig. 5*B*, arrows indicate particle displacements from t_0 to t. Particles' positions at time t are shown and colored according to their kinetic energy. An event typically starts with chain-like rearrangements at the raft edge, the locations of which are correlated with defects that delineate the interface between the raft's core and its outer layers, as shown in Fig. 5 *A*, *i* and *ii* (*SI Appendix*, Fig. S10) (38). Particle motion creates more defects which propagate through the entire extent of the raft (*SI Appendix*, Fig. S11), inducing an avalanche-like burst of collective rearrangement that persists until the kinetic energy is dissipated and the system attains some stable configuration. We note that there is significant spatial heterogeneity in the particle rearrangements during an event, with the most mobile particles tending to collectively move in a one-dimensional path through the raft, similar to what has been observed in glassy supercooled liquids (39–41), crystalline solids near melting (28, 29, 42), or dusty plasmas (23).

However, rather than existing in a kinetically trapped state, our levitated rafts are continuously excited by nonconservative, hydrodynamic interactions. As such, they show no evidence of approaching a quiescent ground state and instead undergo intermittent avalanche-like events indefinitely. The crystal-like configurations before and after events are not distinctly different, evidence that excitations are not driven by configurational relaxation (Fig. 5 *A*, *i* and *ii*, *SI Appendix*, Fig. S12, and Movie S4). Furthermore, avalanche-like events in levitated rafts are not localized and eventually involve the entire system (Fig. 5*B*).

In order to illuminate the nonequilibrium nature of these hydrodynamically driven raft rearrangements, we compare our experimental results with predictions based on a thermal ensemble of particles. To this end, we plot the mean square displacement (MSD) for both the experiment and a molecular dynamics simulation (*SI Appendix*, Fig. S13) with pair-wise interactions

(Fig. 5*C*). To properly compare the data, we nondimensionalize distances by the lattice spacing $L = \langle r \rangle$ and times by the time taken for a particle to ballistically travel a distance of one lattice spacing $t^* = L/\langle v \rangle_{N,t}$. For particles in a thermal bath and with $k_B T/V_B = 0.04$ (the case most analogous to our experiments; see *SI Appendix*, Fig. S13 for details), where V_B is the binding energy, the MSD traces exhibit ballistic behavior for $t \ll t^*$, caging for $t \approx t^*$, and diffusive motion for $t \gg t^*$ (43). In contrast, the experimental MSD does not exhibit any caging behavior. Instead, it transitions directly from ballistic to diffusive behavior around $t \approx 0.1t^*$. This behavior is reminiscent of that of a liquid or gas, without lattice ordering to induce intermediate-time caging. Notably, although the experiment has an effective temperature $\langle E_{kin} \rangle / V_B = 8 \times 10^{-4}$, nearly 50 times lower than the simulation counterpart, the experimental particles are more mobile due to the presence of intermittent avalanches.

To further examine this exotic behavior, we define a velocity-direction correlation parameter

$$\gamma(t) = \sum_{ij} (\hat{n}_i(t) \cdot \hat{n}_j(t)) w_{ij}(t), \qquad [2]$$

where $\hat{n}_i$ and $\hat{n}_j$ are the unit vectors of displacement for neighboring particles i and j, and $\hat{r}_{ij}$ is the displacement unit vector between particles. In addition, we define a weight density $w_{ij}(t) = (\hat{n}_i(t) \cdot \hat{r}_{ij}(t))^2$, indicated by the shading in the schematic of Fig. 5*D*, such that directions parallel to the velocity of the particle are weighted more than those perpendicular. Our results are plotted in Fig. 5*D* and show that the levitated particles display highly correlated motions even at short times, consistent with the predictions of correlated layer shearing shown in Fig. 3*A*. In contrast, the motions of particles in the thermal simulation are uncorrelated and only begin to correlate after the ballistic regime $t > 0.1t^*$. Fundamentally, this contrast highlights the difference between excitations induced by hydrodynamic instabilities and by thermal fluctuation. Hydrodynamic instability–induced excitations stem from the nonconservative, multibody interactions illustrated in Fig. 3*A*, and they therefore display a high degree of spatiotemporal correlation and depend on the configuration of nearby particles.

We show that this spatiotemporal correlation results in the lack of particle caging by measuring the number of particles that escape their caging neighborhood over time. Here, particles are considered to have escaped their cage if they traversed at least one lattice spacing relative to t_0. Our results are plotted in Fig. 5*E* and show that the levitated particles begin to uncage at $t \approx t^*$, which is the time particles will take to cross a distance L if their motion is ballistic. In contrast, the simulated thermal system only starts to uncage for $t \approx 10t^*$, which is when the particle motion becomes diffusive. This distinction shows how the correlated motions make the levitated crystal susceptible to perturbations, as a single uncaging event is amplified into a system-spanning event by the tendency of interparticle hydrodynamic interactions to correlate particle motions.

Taken together, our results establish acoustically levitated rafts as a potent platform for investigating how strong hydrodynamic coupling can spontaneously excite a many-body system. By tuning the relative strength of attractive scattering interactions and repulsive microstreaming flows, particle configurations exhibit hydrodynamic instabilities, which produce nonreciprocal interparticle forces that scale in magnitude with applied acoustic pressure more quickly than any stabilizing acoustic binding. As a consequence, increasing acoustic pressure drives crystalline rafts through a transition involving intermittent periods of spatially correlated, string-like particle rearrangements that eventually merge into a two-dimensional fluid-like steady state. These excitations differ from relaxation events found in supercooled systems (39–41) or in ultrasoft colloidal crystals (42) by their persistent, spontaneous nature. They also appear different from string-like cooperative events in soft fragile crystals triggered by thermal fluctuations (29, 42) since we observe them to appear already in the quiescent lattice state of an athermal raft. This difference with thermal systems is in line with recent results for driven active matter, which showed that to recover thermal-like behavior statistical decorrelation between driven and fluctuating degrees of freedom would be required (44). Levitated rafts may also serve as a suitable system to explore experimentally the link between spatially varying dissipation and dynamic transitions, as seen in simulations of active matter (45, 46). Finally, our results provide valuable insight into the limits of acoustic many-body control, elucidating a key instability mechanism that affects the precision of acoustic manipulation at small scales.

Materials and Methods

Experiment. The acoustic cavity was driven by an ultrasonic transducer with a piezoelectric element onto which an aluminum horn was bolted to amplify the acoustic power generation. The bottom of the metallic horn had a concave radius of curvature $R = 50$ mm and was painted black to minimize light reflection during video imaging. The concave geometry weakly confined the particles at the center of the trap. A heat tape, regulated with a PID temperature controller, was wrapped around the horn and maintained the transducer at 35 ± 0.5 °C for experimental repeatability. The piezoelectric element was driven by applying a sinusoidal wave of peak-to-peak voltage V_{pp} in the range 60–200 V at a frequency close to the resonance frequency of the horn, $\omega_0/(2\pi) = 34.870$ kHz; this signal was generated by a function generator and amplified by a high-voltage amplifier (A-301 HV amplifier, AA Lab Systems). The transparent reflector consisted of a glass plate coated with indium tin oxide (ITO). To reduce the effect of tribocharging, both the horn and reflector were grounded. The gap between the edge of the horn and the reflector could be adjusted to $\lambda_0/2$ by moving the reflector plate with a translation stage, where $\lambda_0 = 9.8$ mm is the wavelength associated with ω_0. Throughout all experiments, we keep the gap height constant ($\lambda_0/2$). In order to minimize the effect of air currents, the entire setup was enclosed within an acrylic box with dimensions much larger than the levitation region ($l \times w \times h = 61 \times 30 \times 46 \times \text{cm}^3$).

We used polyethylene spherical particles (Cospheric, material density $\rho = 1{,}000\ \text{kgm}^{-3}$, diameter $d = 30$ to 60 μm; see *SI Appendix*, Figs. S2 and S3 for particle size distribution). The particles were stored, and all experiments were performed, within a humidity and temperature–controlled laboratory environment (45 to 50 % relative humidity, 22 to 24 °C).

Before and after each experiment, the bottom reflector was cleaned with deionized water and dried with compressed air. For each experiment, the particles were added to the cavity with a tweezer. Videos were recorded with a high-speed camera (Vision Research Phantom T1340) at 3,000 frames per second. The acoustic pressure in the cavity was measured with a laser-based acoustic sensor (Xarion Eta100 Ultra optical microphone).

Particle positions were obtained from a custom tracking algorithm, which utilized the watershed algorithm to separate particles in contact and then used the regionprops algorithm to calculate the centroid of individual particles (performed using algorithms implemented in Matlab version R2021b). Before analysis, any global translation and rotation of the cluster (typically negligible) was subtracted from the xy positions of individual particles (*SI Appendix*, section S14). For each particle, the xy positions were then smoothed by applying a moving average with a window size of 5 frames (≈1.7 ms) to reduce particle tracking noise (usually around 1 pixel = 2.4 μm). The velocity of particle i at time t was then calculated as $v_i(t) = |\vec{r}_i(t) - \vec{r}_i(t - \Delta t)|/\Delta t$, where $\vec{r}_i(t) = (x, y)$ is the position of particle i at time t, and $\Delta t = 0.33$ ms.

Lattice Boltzmann Simulation. The lattice Boltzmann method (LBM) was used to perform simulations of particles interacting through acoustically mediated forces. This method captures the full extent of the fluid–structure interactions, naturally including the effects of viscous dissipation and momentum transfer due to multiple scattering events. LBM simulations of the acoustic cavity were performed within the waLBerla framework (47). A single relaxation time scheme with a viscosity matching that of air was used (48). Particles were simulated in periodic domains to avoid spurious boundary reflections. A spatially homogeneous background force field was used to oscillate the background fluid. The PE functionality of the waLBerla framework was used to simulate the interaction of particles with the acoustic field (49). Hydrodynamic forces between the particles and fluid were handled with the partially saturated cells method (50). A local cell size of $D/15$, where D is the particle diameter, provided sufficiently high lattice resolution for accurate force calculations.

COMSOL Simulation. COMSOL Multiphysics Software was used to perform finite element simulation of particles interacting in acoustic cavity. Solutions were obtained by first solving the linearized Navier–Stokes equation utilizing the Thermoviscous Acoustics, Frequency Domain module. This method considers viscous effects and properly resolves the acoustic boundary layer. Next, the second-order time-averaged net flow was solved by adding the necessary source terms (from the first-order fields) to the Laminar Flow interface (51). The solution obtained is the steady-state solution at long times and free from any transients. Particles were simulated in a rectangular box of height $10D$ and width $40D$. The top and bottom walls were actuated in phase with a fixed displacement amplitude and frequency. The side walls of the simulation box had periodic boundary conditions to avoid reflections and other finite size effects. The minimal and maximal mesh sizes used around a particle were 0.6 μm and 9.5 μm, respectively, to resolve viscous and streaming effects appropriately.

Data, Materials, and Software Availability. All data are available at https://doi.org/10.18126/FJHL-CY15 (52).

ACKNOWLEDGMENTS. We thank Nina Brown, Tali Khain, Qinghao Mao, Severine Atis, and Justin Burton for useful and inspiring discussions. This research was supported by the NSF through award number DMR-2104733. The work utilized the shared experimental facilities at the University of Chicago MRSEC, which is funded by the NSF under award number DMR-2011854. The research also benefited from computational resources and services supported by the Research Computing Center at the University of Chicago.

1. A. Marzo *et al*., Holographic acoustic elements for manipulation of levitated objects. *Nat. Commun.* **6**, 8661 (2015).
2. G. Memoli *et al*., Metamaterial bricks and quantization of meta-surfaces. *Nat. Commun.* **8**, 14608 (2017).
3. D. Foresti, M. Nabavi, M. Klingauf, A. Ferrari, D. Poulikakos, Acoustophoretic contactless transport and handling of matter in air. *Proc. Natl. Acad. Sci. U.S.A.* **110**, 12549–12554 (2013).
4. T. M. Llewellyn-Jones, B. W. Drinkwater, R. S. Trask, 3D printed components with ultrasonically arranged microscale structure. *Smart Mater. Struct.* **25**, 02LT01 (2016).
5. K. Melde, A. G. Mark, T. Qiu, P. Fischer, Holograms for acoustics. *Nature* **537**, 518–522 (2016).
6. D. Ahmed *et al*., Rotational manipulation of single cells and organisms using acoustic waves. *Nat. Commun.* **7**, 11085 (2016).
7. Q. Shi *et al*., A general approach to free-standing nanoassemblies via acoustic levitation self-assembly. *ACS Nano.* **13**, 5243–5250 (2019).
8. Z. Chen *et al*., Liquid marble coalescence and triggered microreaction driven by acoustic levitation. *Langmuir* **33**, 6232–6239 (2017).
9. S. Tsujino, T. Tomizaki, Ultrasonic acoustic levitation for fast frame rate X-ray protein crystallography at room temperature. *Sci. Rep.* **6**, 25558 (2016).
10. M. X. Lim, A. Souslov, V. Vitelli, H. M. Jaeger, Cluster formation by acoustic forces and active fluctuations in levitated granular matter. *Nat. Phys.* **15**, 460–464 (2019).
11. M. X. Lim, B. VanSaders, A. Souslov, H. M. Jaeger, Mechanical properties of acoustically levitated granular rafts. *Phys. Rev. X* **12**, 021017 (2022).
12. R. Y. Dong, W. Wang, S. Granick, Colloidal flatlands confronted with urge for the third dimension. *ACS Nano* **13**, 9442–9448 (2019).
13. M. A. Abdelaziz *et al*., Ultrasonic chaining of emulsion droplets. *Phys. Rev. Res.* **3**, 043157 (2021).
14. G. T. Silva, H. Bruus, Acoustic interaction forces between small particles in an ideal fluid. *Phys. Rev. E* **90**, 063007 (2014).
15. J. Rudnick, M. Barmatz, Oscillational instabilities in single-mode acoustic levitators. *Acoust. Soc. Am. J.* **87**, 81–92 (1990).
16. M. A. B. Andrade, S. Polychronopoulos, G. Memoli, A. Marzo, Experimental investigation of the particle oscillation instability in a single-axis acoustic levitator. *AIP Adv.* **9**, 035020 (2019).
17. I. M. Jánosi, T. Tél, D. E. Wolf, J. A. C. Gallas, Chaotic particle dynamics in viscous flows: The three-particle Stokeslet problem. *Phys. Rev. E* **56**, 2858–2868 (1997).
18. R. Chajwa, N. Menon, S. Ramaswamy, Kepler orbits in pairs of disks settling in a viscous fluid. *Phys. Rev. Lett.* **122**, 224501 (2019).
19. C. C. Thomas, J. P. Gollub, Structures and chaotic fluctuations of granular clusters in a vibrated fluid layer. *Phys. Rev. E* **70**, 061305 (2004).
20. M. Chaudhuri, A. V. Ivlev, S. A. Khrapak, H. M. Thomas, G. E. Morfill, Complex plasma–The plasma state of soft matter. *Soft Matter* **7**, 1287–1298 (2011).
21. L. I, W. T. Juan, C. H. Chiang, J. H. Chu, Microscopic particle motions in strongly coupled dusty plasmas. *Science* **272**, 1626–1628 (1996).
22. S. Nunomura, D. Samsonov, S. Zhdanov, G. Morfill, Self-diffusion in a liquid complex plasma. *Phys. Rev. Lett.* **96**, 015003 (2006).
23. C. Yang, W. Wang, L. I, Avalanche structural rearrangement through cracking-healing in weakly stressed cold dusty plasma liquids. *Phys. Rev. E* **93**, 013202 (2016).
24. H. W. Hu, Y. C. Zhao, L. I, Avalanche structural rearrangements in cold dusty plasma liquids through cascaded coherent excitations of heterogeneous multiscale thermal acoustic waves. *Phys. Rev. Res.* **4**, 023116 (2022).
25. G. Gogia, J. C. Burton, Emergent bistability and switching in a nonequilibrium crystal. *Phys. Rev. Lett.* **119**, 178004 (2017).
26. K. Zahn, G. Maret, Dynamic criteria for melting in two dimensions. *Phys. Rev. Lett.* **85**, 3656–3659 (2000).
27. A. L. Thorneywork, J. L. Abbott, D. G. Aarts, R. P. Dullens, Two-dimensional melting of colloidal hard spheres. *Phys. Rev. Lett.* **118**, 158001 (2017).
28. Y. Wang *et al*., Electronically driven 1D cooperative diffusion in a simple cubic crystal. *Phys. Rev. X* **11**, 011006 (2021).
29. X. Wang, X. Tong, H. Zhang, J. F. Douglas, String-like collective motion and diffusion in the interfacial region of ice. *J. Chem. Phys.* **147**, 194508 (2017).
30. L. V. King, On the acoustic radiation pressure on spheres. *Proc. R. Soc. London. Ser. A: Math. Phys. Sci.* **147**, 212–240 (1934).
31. L. P. Gor'kov, On the forces acting on a small particle in an acoustical field in an ideal fluid. *Sov. Phys. Dokl.* **6**, 773 (1962).
32. C. A. Lane, Acoustical streaming in the vicinity of a sphere. *J. Acoust. Soc. Am.* **27**, 1082–1086 (1955).
33. D. Fabre, J. Jalal, J. S. Leontini, R. Manasseh, Acoustic streaming and the induced forces between two spheres. *J. Fluid Mech.* **810**, 378–391 (2017).
34. D. Klotsa, M. R. Swift, R. M. Bowley, P. J. King, Chain formation of spheres in oscillatory fluid flows. *Phys. Rev. E* **79**, 021302 (2009).
35. G. A. Voth *et al*., Ordered clusters and dynamical states of particles in a vibrated fluid. *Phys. Rev. Lett.* **88**, 234301 (2002).
36. F. Otto, E. K. Riegler, G. A. Voth, Measurements of the steady streaming flow around oscillating spheres using three dimensional particle tracking velocimetry. *Phys. Fluids* **20**, 093304 (2008).
37. A. V. Ivlev *et al*., Statistical Mechanics where Newton's Third Law is Broken. *Phys. Rev. X* **5**, 011035 (2015).
38. M. Kong, B. Partoens, F. M. Peeters, Topological defects and nonhomogeneous melting of large two-dimensional Coulomb clusters. *Phys. Rev. E* **67**, 021608 (2003).
39. A. Widmer-Cooper, P. Harrowell, H. Fynewever, How reproducible are dynamic heterogeneities in a supercooled liquid? *Phys. Rev. Lett.* **93**, 135701 (2004).
40. A. S. Keys, A. R. Abate, S. C. Glotzer, D. J. Durian, Measurement of growing dynamical length scales and prediction of the jamming transition in a granular material. *Nat. Phys.* **3**, 260–264 (2007).
41. C. Reichhardt, C. J. Olson Reichhardt, Fluctuating topological defects in 2D liquids: Heterogeneous motion and noise. *Phys. Rev. Lett.* **90**, 095504 (2003).
42. B. van der Meer *et al*., Highly cooperative stress relaxation in two-dimensional soft colloidal crystals. *Proc. Natl. Acad. Sci. U.S.A.* **111**, 15356–15361 (2014).
43. E. R. Weeks, D. A. Weitz, Subdiffusion and the cage effect studied near the colloidal glass transition. *Chem. Phys.* **284**, 361–367 (2002).
44. M. Han *et al*., Fluctuating hydrodynamics of chiral active fluids. *Nat. Phys.* **17**, 1260–1269 (2021).
45. F. Cagnetta, F. Corberi, G. Gonnella, A. Suma, Large fluctuations and dynamic phase transition in a system of self-propelled particles. *Phys. Rev. Lett.* **119**, 158002 (2017).
46. L. Tociu, É. Fodor, T. Nemoto, S. Vaikuntanathan, How dissipation constrains fluctuations in nonequilibrium liquids: Diffusion, structure, and biased interactions. *Phys. Rev. X* **9**, 041026 (2019).
47. M. Bauer *et al*., waLBerla: A block-structured high-performance framework for multiphysics simulations. *Comput. Math. Appl.* **81**, 478–501 (2021).
48. D. Yu, R. Mei, L. S. Luo, W. Shyy, Viscous flow computations with the method of lattice Boltzmann equation. *Prog. Aerosp. Sci.* **39**, 329–367 (2003).
49. J. Götz, K. Iglberger, C. Feichtinger, S. Donath, U. Rüde, Coupling multibody dynamics and computational fluid dynamics on 8192 processor cores. *Parallel Comput.* **36**, 142–151 (2010).
50. D. Owen, C. Leonardi, Y. Feng, An efficient framework for fluid–structure interaction using the lattice Boltzmann method and immersed moving boundaries. *Int. J. Numer. Methods Eng.* **87**, 66–95 (2011).
51. P. B. Muller, H. Bruus, Numerical study of thermoviscous effects in ultrasound-induced acoustic streaming in microchannels. *Phys. Rev. E* **90**, 043016 (2014).
52. B. Wu, B. VanSaders, M. X. Lim, H. M. Jaeger, Dataset for Hydrodynamic Coupling Melts Acoustically Levitated Crystalline Rafts. MDF Open. https://doi.org/10.18126/FJHL-CY15. Accessed 28 June 2023.